Clays and Clay Minerals, Vol. 60, No. 2, 121–135, 2012.

Ni ENRICHMENT AND STABILITY OF Al-FREE GARNIERITE SOLID-SOLUTIONS: A THERMODYNAMIC APPROACH

S. GALÍ[1,*], J. M. SOLER[2], J. A. PROENZA[1], J. F. LEWIS[3], J. CAMA[2], AND E. TAULER[1]

[1] Department of Crystallography, Mineralogy and Mineral Deposits, Faculty of Geology, University of Barcelona, C/ Martí i Franquès S/N, 08028, Barcelona, Catalonia, Spain

[2] Institute of Environmental Assessment and Water Research, IDAEA, CSIC, Jordi Girona 18-26, 0803, Barcelona, Catalonia, Spain

[3] Department of Earth and Environmental Sciences, The George Washington University, Washington, D.C. 20052 USA

Abstract—Garnierites represent significant Ni ore minerals in the many Ni-laterite deposits worldwide. The occurrence of a variety of garnierite minerals with variable Ni content poses questions about the conditions of their formation. From an aqueous-solution equilibrium thermodynamic point of view, the present study examines the conditions that favor the precipitation of a particular garnierite phase and the mechanism of Ni-enrichment, and gives an explanation to the temporal and spatial succession of different garnierite minerals in Ni-laterite deposits. The chemical and structural characterization of garnierite minerals from many nickel laterite deposits around the world show that this group of minerals is formed essentially by an intimate intermixing of three Mg-Ni phyllosilicate solid solutions: serpentine-népouite, kerolite-pimelite, and sepiolite-falcondoite, without or with very small amounts of Al in their composition. The present study deals with garnierites which are essentially Al-free. The published experimental dissolution constants for Mg end-members of the above solid solutions and the calculated constants for pure Ni end-members were used to calculate Lippmann diagrams for the three solid solutions, on the assumption that they are ideal. With the help of these diagrams, congruent dissolution of Ni-poor primary minerals, followed by equilibrium precipitation of Ni-rich secondary phyllosilicates, is proposed as an efficient mechanism for Ni supergene enrichment in the laterite profile. The stability fields of the solid solutions were constructed using [log $a_{SiO_2(aq)}$, log $((a_{Mg^{2+}} + a_{Ni^{2+}})/(a_{H^+})^2)$] (predominance) diagrams. These, combined with Lippmann diagrams, give an almost complete chemical characterization of the solution and the precipitating phase(s) in equilibrium. The temporal and spatial succession of hydrous Mg-Ni phyllosilicates encountered in Ni-laterite deposits is explained by the small mobility of silica and the increase in its activity.

Key Words—Garnierites, Kerolite-Pimelite, Ni-laterite, Sepiolite-Falcondoite, Serpentine-Népouite, Stability.

INTRODUCTION

Nickel laterites are regolith materials derived from ultramafic rocks (Trescases, 1975; Golightly, 1981; Brand *et al.*, 1998). Weathering of the rocks results in enriched horizons, so that minor elements such as Ni, Co, and Mn contained in the unaltered parent rock become enriched in the laterite profiles (Brand *et al.*, 1998; Freyssinet *et al.*, 2005; Golightly, 2010). An iron cap (ferricrete or duricrust) is often found at the top of the weathering profile and the cap grades downward through a transitional zone of limonite to a saprolite zone transitional into bed rock. Saprolite is a zone of rapid change and of maximum supergene enrichment of nickel. The protolith or bedrock is mainly dunite, harzburgite, or lherzolite and their serpentinized equivalents.

Following Golightly (1981), Ni laterites are developed from: (1) unserpentinized peridotite (*e.g.* Poro, New Caledonia; Soroako West, Indonesia); (2) partially serpentinized peridotite (*e.g.* Falcondo Mine, Dominican Republic); or (3) totally serpentinized parent rock (*e.g.* Bonsora, Soroako East, Indonesia). As an example, selected analyses for the most important primary Ni-carrying minerals at Falcondo (Table 1) indicate that these minerals are mainly olivine and 'oceanic' serpentine. The fate of Ni can be tracked through the different values of the atomic ratio of Fe/Ni in these minerals. Initially, in olivine, Fe/Ni $\approx$ 19. In oceanic serpentines this value is slightly smaller, indicating that some of the Fe is relocated in other phases like maghemite, which is readily hydrated to goethite. Goethite is able to incorporate or attach Ni (Manceau *et al.*, 2003). The nickel contained in the limonite horizon and in primary serpentines is transferred to percolating meteoric solutions, and moves downward through the profile, being concentrated with Si and Mg within the underlying saprolite horizon to form secondary Ni-enriched phyllosilicates.

In many Ni lateritic deposits of the hydrous silicate type, the lower saprolite is the ore horizon, and the ore minerals are mainly nickeloan varieties of serpentine,

* E-mail address of corresponding author:
gali@ub.edu
DOI: 10.1346/CCMN.2012.0600203

Table 1. Selected analyses of primary minerals in the parent rock of the Falcondo Ni-laterite deposit (Dominican Republic). Chr: accesory chromite, Ol: olivine, Opx: orthopyroxene, Cpx: clinopyroxene, and Srp: oceanic serpentine.

	1	2	3	4	5	6	7	8	9	10
	— Chr —		— Ol —		— Opx —		— Cpx —		— Srp —	
Wt.%										
SiO_2	0.10	0.11	41.25	40.94	57.09	56.32	53.16	53.22	42.14	40.82
TiO_2	0.14	0.00	0.03	0.02	0.05	0.04	0.79	0.82	0.00	0.00
Al_2O_3	6.92	32.44	0.00	0.00	2.53	3.41	2.39	2.40	0.01	0.00
Cr_2O_3	63.27	34.10	0.01	0.01	0.51	0.71	0.90	0.91	0.03	0.00
Fe_2O_3(c)	1.21	1.76			0.00	0.00	0.13	0.00		
FeO	17.45	17.09	8.81	9.23	6.70	6.28	4.67	4.83	3.92	5.23
V_2O_3	0.16	0.29	–		–		–	–	–	–
MnO	0.28	0.21	0.10	0.17	0.15	0.16	0.16	0.14	0.04	0.03
MgO	10.10	12.66	50.00	49.81	32.98	32.87	17.08	16.97	40.42	40.31
CaO	–	–	0.01	0.00	0.78	0.96	21.19	21.10	0.00	0.02
Na_2O	–	–	–		0.01	0.01	0.40	0.38	0.00	0.00
K_2O	–	–	–		0.00	0.00	0.00	0.00	0.00	0.02
ZnO	0.16	0.30	–		–	–	–	–	–	–
NiO	0.04	0.02	0.40	0.46	–	–	–	–	0.26	0.32
H_2O									12.79	12.67
Total	99.84	98.98	100.61	100.64	100.80	100.76	100.88	100.78	99.64	99.43

talc, sepiolite, chlorite, or smectites, many of which are poorly defined and informally named "garnierites" (*e.g.* Brindley and Hang, 1973; Springer, 1974; Pelletier, 1983). Garnierite is generally used as a field term referring to a wide variety of Ni-bearing hydrous silicates with a characteristic green color (*e.g.* Gleeson *et al.*, 2003). When only small amounts of Al are present in the protolith, garnierites can be formed by different combinations of the three main Mg–Ni solid solutions with serpentine, talc, and sepiolite-like structures; clays (chlorites and smectites) being absent (Wells *et al.*, 2009; Tauler *et al.*, 2009; Villanova-de-Benavent *et al.*, 2011a).

Garnierites occur filling fractures, featureless voids, and cavities or as interstitial veins in the joints separating serpentine blocks, most commonly in the lower part of the saprolite horizon. Often, they have been removed from their original emplacement and have accumulated in cavities, forming breccias (Cluzel and Vigier, 2008). The most common and most studied occurrences of garnierites are found in the less serpentinized ophiolite-related peridotites of mantle origin as in New Caledonia (Trescases, 1975; Wells *et al.*, 2009) and in the Caribbean (Gleeson *et al.*, 2003; Lewis *et al.*, 2006).

The progressive enrichment of Ni in the saprolite horizon occurs by means of two different processes. The dominant process is the direct replacement of pre-weathering minerals, such as olivine and serpentine, by NiFe-enriched lizardites and by Ni-rich smectites. In the minerals formed by replacement, Fe and Ni increase at a percentage range (see Table 1). The second process involves the precipitation of Mg-Ni phyllosilicates (Al-free garnierites) from aqueous solution. As described above, the garnierites form as fracture fillings, veins, and breccias. In contrast to the minerals formed by replacement, the garnierites are characterized by low Fe and are essentially free of Al. These garnierite minerals and the conditions of the precipitation process by which they form are the subject of the present study.

Here the authors explain, using equilibrium thermodynamics, three related, simultaneous phenomena: (1) supergene enrichment of Ni in a group of secondary phyllosilicates precipitating in Ni-laterite profiles – Lippmann's diagrams (Lippmann, 1980) were found to be very helpful for this; (2) simultaneous precipitation of Mg-Ni-phyllosilicate solid solutions (in theory, up to three different s.s. ± quartz) – this can be represented by an activity diagram proposed below; and (3) the spatial and temporal evolution of garnierites towards more silica-rich members, from serpentine to talc and sepiolite-type minerals, as has been described previously (*e.g.* Golightly, 1981; Freyssinet *et al.*, 2005).

A simplified chemical system which is useful in the description of the stability relations among the Ni-containing phyllosilicate phases consists of four components: MgO, NiO, SiO_2, and H_2O. For aqueous solutions the basic species are: Mg^{2+}, Ni^{2+}, SiO_2(aq), H^+, and H_2O. As garnierites are Fe-poor (<0.5 wt.% Fe) indicating a secondary origin (Pelletier, 1983; Manceau and Calas, 1985; Manceau *et al.*, 1985; Proenza *et al.*, 2008; Wells *et al.*, 1999), Fe was not included in the system. Its inclusion would increase the complexity of the system without affording significant new information regarding the distribution of Ni among the main phases present. After weathering, residual Fe of the parent rock is concentrated in a highly insoluble limonitic horizon, formed mainly of goethite, hematite, and maghemite.

This horizon is best defined by the complete disappearance of the primary silicates and is distinct from the heterogeneous saprolite below.

The Mg-Ni-phyllosilicates are members of three solid-solution series extending from Mg and Ni end-members (*e.g.* Springer, 1974, 1976; Brindley *et al.*, 1979; Gleeson *et al.*, 2003; Tauler *et al.*, 2009; Wells *et al.*, 2009; Reddy *et al.*, 2009; Villanova-de-Benavent *et al.*, 2011b). The electron microprobe (EMP) analyses plotted in Figure 1 confirm this; a complete, stable solid solution between Mg and Ni end-members in the structures of these minerals must be possible at atmospheric temperatures and pressure.

Therefore, a complete solid solution between Mg and Ni end-members is a reasonable hypothesis. The terminology used here for the end-members, composition, and structure for the solid solutions are: serpentine ($Mg_3Si_2O_5(OH)_4$), népouite ($Ni_3Si_2O_5(OH)_4$); kerolite (or hydrated talc) ($Mg_3Si_4O_{10}(OH)_2{\cdot}H_2O$), pimelite (or hydrated willemseite) ($Ni_3Si_4O_{10}(OH)_2{\cdot}H_2O$); and sepiolite ($Mg_8Si_{12}O_{30}(OH)_4(H_2O)_4{\cdot}8H_2O$) falcondoite ($Ni_8Si_{12}O_{30}(OH)_4(H_2O)_4{\cdot}8H_2O$) (Brindley and Hang, 1973; Brindley and Maksimovic, 1974; Springer, 1974; Brindley and Wan, 1975; Brindley *et al.*, 1979). Serpentine in saprolite can be present as a mixture of different structural varieties such as chrysotile, clinochrysotile, polygonal serpentine, and lizardite-1*T*. Indeed, in a single nanoscale particle, the transition between the different structural varieties can be observed using transmission electron microscopy (TEM) (Villanova-de-Benavent *et al.*, 2011a). Kerolite and Ni-rich kerolite, a very fine-grained, hydrated variety of talc, is also present (Brindley *et al.*, 1979; Soler *et al.*, 2008).

Here, the published experimental dissolution constants for Mg end-members and the calculated constants for pure Ni end-members were used to calculate Lippmann diagrams for the serpentine-népouite, kerolite-pimelite, and sepiolite-falcondoite (Srp-Nep, Ker-Pim, and Sep-Fal) solid solutions, on the assumption that they are ideal. In addition a particular activity diagram for the system $MgO–NiO–SiO_2–H_2O$, delimiting the stability field of each Ni-bearing phyllosilicate and quartz, is proposed. Garnierites, as described below, can precipitate from aqueous solution in the form of one or two solid solutions, under near equilibrium conditions.

THEORY

The basic reactions involved in the formation or dissolution of Mg and Ni end-member silicates are given in Table 2. In the system $MgO–NiO–SiO_2–H_2O$, under constant temperature and pressure, the maximum number of phases present in equilibrium is four. In the presence of an aqueous phase, three solid phases are in equilibrium for zero degrees of freedom. Hence, in garnierites, a maximum of either three solid solutions or two solid solutions plus quartz is expected to precipitate from solution under near-equilibrium conditions. However, the most frequent observation is the existence of equilibrium between two solids (two solid solutions or one solid solution and quartz), or simply a single solid

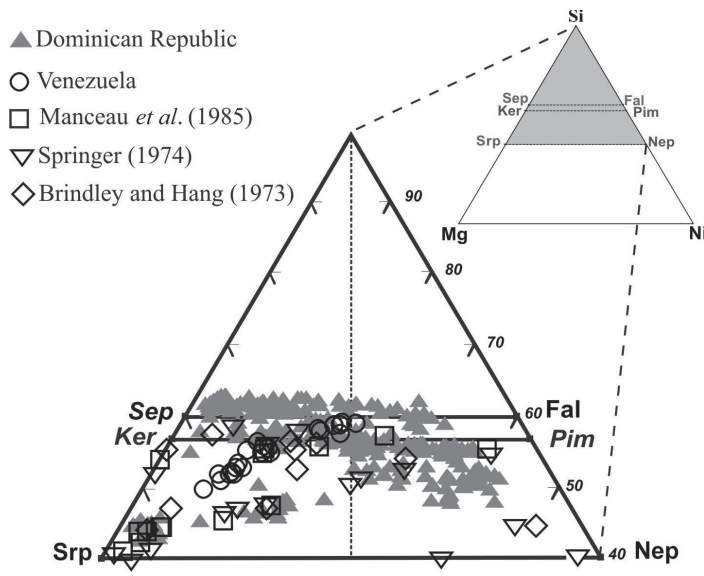

Figure 1. Projection of Caribbean garnierite ore compositions (Proenza *et al.*, 2008; Tauler *et al.*, 2009; Soler *et al.*, 2010; Villanova-de-Benavent *et al.*, 2011a, 2011b) and published data (Brindley and Hang, 1973; Brindley, and Wan, 1975; Springer, 1974, 1976; Manceau *et al.*, 1985) for garnierites from different Ni-laterite deposits, in a Si–Ni–Mg ternary diagram (at.%). The positions of the solid-solution series between Ni-sepiolite (Sep)-falcondoite (Fal), kerolite (Ker)-pimelite (Pim), and lizardite (Srp)-népouite (Nep) are also indicated.

Table 2. Dissolution reactions for Mg and Ni end-members of garnierite, phyllosilicates, and quartz, labeled with the corresponding equilibrium constants used in the text.

Serpentine: $Mg_3Si_2O_5(OH)_4 + 6\ H^+ = 3\ Mg^{+2} + 2\ SiO_2(aq) + 5\ H_2O$	log K1 (1)
Népouite: $Ni_3Si_2O_5(OH)_4 + 6\ H^+ = 3\ Ni^{+2} + 2\ SiO_2(aq) + 5\ H_2O$	log K2 (2)
Kerolite: $Mg_3Si_4O_{10}(OH)_2{\cdot}H_2O + 6\ H^+ = 3\ Mg^{+2} + 4\ SiO_2(aq) + 5\ H_2O$	log K3 (3)
Pimelite: $Ni_3Si_4O_{10}(OH)_2{\cdot}H_2O + 6\ H^+ = 3\ Ni^{+2} + 4\ SiO_2\ (aq) + 5\ H_2O$	log K4 (4)
Sepiolite: $Mg_8Si_{12}O_{30}(OH)_4(H_2O)_4{\cdot}8H_2O + 16\ H^+ = 8\ Mg^{+2} + 12\ SiO_2(aq) + 22\ H_2O$	log K5 (5)
Falcondoite: $Ni_8Si_{12}O_{30}(OH)_4(H_2O)_4{\cdot}8H_2O + 16\ H^+ = 8\ Ni^{+2} + 12\ SiO_2(aq) + 22\ H_2O$	log K6 (6)
Quartz: SiO_2 (quartz) = $SiO_2(aq)$	(7)

that is a solid solution or quartz (*e.g.* Vitovskaya *et al.*, 1969; Brindley and Hang, 1973; Springer, 1974; Golightly, 1981; Soler *et al.*, 2008, and examples in the present study).

With the given reactions (Table 2), all possible combinations of phases can be examined in light of thermodynamic considerations, provided that the corresponding equilibrium constants are known. A brief account of the equilibrium constants used was necessary, before the different combinations of phases in the system were reviewed. The most problematic choice was for the equilibrium constant of reaction (1) (Table 2), (log K1 value). Several log K constants for the dissolution of serpentine are found in the literature (Table 3), and most are controversial because of the different crystal structures of serpentines and the close proximity of these structures in the same sample (Evans, 2004). The various equilibrium constants were calculated from the respective free energies of formation (Table 4). The value of log K1 (for reaction 1) was constrained by the experimental observation that at equilibrium Ni-kerolitie was more enriched in Ni than Ni-serpentine. The log K1 value that best fits the observed compositions of this equilibrium is the one derived from $\Delta G_{serpentine}$ given by Bricker *et al.* (1973). Constant values for Mg end-members of kerolite and sepiolite (log K3 and log K5)

Table 3. Reported and calculated log K values.

Structure	ΔG_f (kJ/mol)	log K	Reference
Serpentine minerals			
Chrysotile	−4037.02	31.86	Helgeson *et al.* (1978)
Serpentine	−4038.25	31.64	Golightly (1981)
Chrysotile	−4042.64	30.87	Mel'nik (1972)
Chrysotile	−4027.07	33.60±0.41	Bricker *et al.* (1973)
Chrysotile	−4038.96	31.51	Hostetler and Christ (1968)
Nepouite	−2866.69	21.4688	This work, from Nriagu (1975)
	−2883.20	18.58	Golightly (1981)
Talc structure			
Well crystallized	−5524.9	21.73	Helgeson *et al.* (1978)
Poorly crystallised	−5504.4	25.33	Tardy and Duplay (1992)
Kerolite	−5736.70	25.79±0.24	Stoessell (1988)
Pimelite	−4591.24	11.46	Tthis work, from Nriagu (1975)
	−4594.67	10.85	Golightly (1981)
Sepiolite	−4271.61	15.53	from Christ *et al.* (1973)
Sepiolite	−4387.05	15.76*	Stoessell (1988)
Falcondoite	−3505.36	6.1565*	This work, from Nriagu (1975)

* These constants correspond to the formula of sepiolite used by Stoessell, based on two octahedral cations. The underlined log K values were used in the present work.

Table 4. Free energies of formation used in the approximations of ΔG_f of the minerals listed in Table 3 and in the derivation of the corresponding log K of dissolution (kJ mol^{-1}).

Species	ΔG_f (kJ/mol)	Uncertainty	Reference
$Mg(OH)_2$	−846.034	0.3	Helgeson (1969)
$Ni(OH)_2$	−459.266	0.2	Tardy and Garrels (1974)
$Si(OH)_4$	−1333.60	1.0	Wagman *et al.* (1968)
H_2O	−237.293	0.04	Wagman *et al.* (1968)
Mg^{+2}	−454.997	0.2	Wagman *et al.* (1968)
Ni^{+2}	−45.123	0.2	Tardy and Garrels (1974)
SiO_2(aq)	−833.70	0.5	Phillips *et al.* (1988)

were taken from dissolution experiments (Stoessell, 1988). The constants for the Ni end-members (népouite, pimelite, and falcondoite) were derived from ΔG_f values calculated by the method proposed by Nriagu (1975), (log K2, log K4, and log K6). Log K values predicted by this model are in good agreement with available experimental data on Mg phases, encouraging the extension of the method to inaccessible phases such as pure Ni phyllosilicate end-members. The error estimated, <1 unit in log K, does not impede the evaluation of the relative stabilities of these phases.

Two-phase equilibria (one solid solution and one aqueous solution)

The simplest situation is when only one Mg-Ni-phyllosilicate solid solution precipitates from an aqueous solution. Equilibria between one solid solution and the aqueous solution were plotted in a Lippmann phase diagram (Lippmann, 1980; Glynn and Reardon, 1990; Prieto, 2009). In these diagrams, the aqueous solution in equilibrium with two (or more) end-member components of a solid solution is described by the "total solubility product" ΣΠeq, (or logΣΠeq), represented on the ordinate, whereas on the abscissa two different variables are depicted: the mole fraction in the solid solution (represented here by X_{Mg}) and the activity fraction in the aqueous solution, $X_{Mg^{2+}}$. ΣΠeq as a function of X_{Mg} and $X_{Mg^{2+}}$ defines the 'solidus' and the 'solutus' curves, respectively. In equilibrium, every ΣΠeq corresponds to an X_{Mg} value and an $X_{Mg^{2+}}$ value (both connected by a horizontal tie-line). An exception is made for pure end-members or alyotropic points where the two values coincide, or when a miscibility gap exists in the solid solution. In general, the variable ΣΠ defines a state of supersaturation, equilibrium, or undersaturation. When ΣΠ lies above the solutus curve, the solution is supersaturated with respect to a series of solid compositions; below the solutus, the solution is undersaturated with respect to all possible compositions of the solid solution.

On the same diagrams, 'minimum stoichiometric saturation curves', MSS, can be depicted. These curves are useful for illustrating the relations between the composition of a given solid solution and the ΣΠ values of the solution when a congruent dissolution occurs. For mineral solid solutions with low solubility, dissolution that occurs congruently is expected, whereas precipitation is likely to occur in equilibrium or under supersaturation conditions. As discussed below, Lippmann diagrams can help to portray the supergene enrichment of Ni in phyllosilicates.

Lippmann diagrams (Figure 2a, 2b, 2c) for Mg-Ni solid solution in serpentine, kerolite, and sepiolite were calculated on the basis of the log K values given above and assuming ideal solid solutions. Note that these curves were calculated for the reduced formula unit of the minerals involved, so that only one octahedral atom enters the formula unit. This amounts to dividing the conventional formulae corresponding to serpentine-népouite and kerolite-pimelite solid solutions by three and dividing those corresponding to the sepiolite-falcondoite series by eight. Log K values for the dissolution reactions were also divided by the corresponding factors. The main reason for using reduced formulae was that the authors applied a 'mixing on sites' model to solid solutions rather than a molecular mixing model. With the reduced formulae, the equilibrium constants for the dissolution reactions and ionic activity product (IAP) for solutions are simpler and the exponents on the activities of substituting ions are unnecessary. The mole fractions in the solid, X_{Mg}, and the activity fractions in solution, $X_{Mg^{2+}}$, represented on the abscissa are given by:

$$X_{Mg} = \frac{N_{Mg}}{N_{Mg} + N_{Ni}}$$

$$X_{Mg^{2+}} = \frac{a_{Mg^{2+}}}{a_{Mg^{2+}} + a_{Ni^{2+}}} \quad (1)$$

where N_{Mg} and N_{Ni} represent moles of Mg and Ni in the solid, and $a_{Mg^{2+}}$ and $a_{Ni^{2+}}$ are the activities of Mg^{2+} and Ni^{2+}, respectively, in solution.

The large contrast between the log K values corresponding to end-members of the solutions is reflected in the 'rectangular' rather than 'narrow loop'

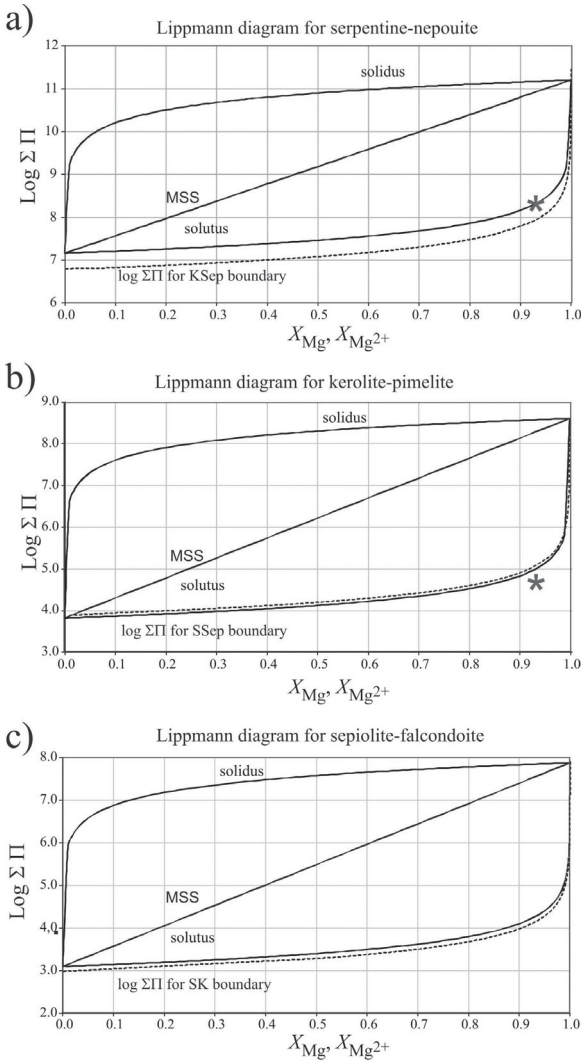

Figure 2. Lippmann diagrams for solid solutions: (a) serpentine-népouite, (b) kerolite-pimelite, and (c) sepiolite-falcondoite. Diagrams show solidus, minimum stoichiometric saturation (MSS), and solutus curves (continuous lines). Dotted curves give the log ΣΠ values corresponding to the two-solid solution boundaries (see text and Figure 6). Asterisks in Figure 2a and 2b are translations of point (−5.5, 12) in Figure 3 into Lippmann's diagram for serpentine-népouite and kerolite-pimelite.

aspect to the solidus and solutus curves (Figure 2a, 2b, 2c). The contrast also explains the efficiency of the supergene enrichment by the mechanism of congruent dissolution-equilibrium precipitation.

In order to use the calculated Lippmann diagrams in a semi-quantitative approach, the possible initial activity ratios of Mg^{2+} and Ni^{2+} in aqueous solution are compared with the resulting mole fractions of these metals in the enriched phases. The following example explains Ni enrichment using the Lippmann diagram (Figure 2a). The values of the ratios $Ni^{2+}/(Mg^{2+} + Ni^{2+})$ in solution from congruent dissolution of primary serpentine ranges between 10^{-3} and 10^{-5} or less. The corresponding tie lines between the solutus and the solidus give the composition of the enriched precipitating solid solution with compositions in the range $Mg_{0.4-2.4}Ni_{2.6-0.6}Si_2O_5(OH)_4$, which reflects much more Ni enrichment compared to the primary serpentine. These compositions are reasonable and representative of the amount of Ni incorporated into a neoformed phase in a single step of the dissolution-precipitation cycle. The repetition of several cycles of congruent dissolution-equilibrium precipitation depends on the hydrological regime in the soil (*i.e.* alternating dry and wet periods, fluctuations in the level of water table, *etc.*), and would produce more and more enriched phases. From one cycle to the next, the enriched precipitating phase type may change depending on the variation in silica activity that will determine the enriched precipitating phase type. For example, if the dissolving phase is a Ni-serpentine and the silica activity increases, the next precipitating phase may be a Ni-kerolite and so on.

The factors included in the calculation of logΣΠeq were $\log(a_{SiO_2(aq)})$ and $\log((a_{Mg^{2+}} + a_{Ni^{2+}})/(a_{H^+})^2)$, so that:

$$\log\Sigma\Pi_{serpentine} = \log((a_{Mg^{2+}} + a_{Ni^{2+}})/(a_{H^+})^2) + (2/3)\cdot\log(a_{SiO_2(aq)}) \quad (2)$$

$$\log\Sigma\Pi_{kerolite} = \log((a_{Mg^{2+}} + a_{Ni^{2+}})/(a_{H^+})^2) + (4/3)\cdot\log(a_{SiO_2(aq)}) \quad (3)$$

$$\log\Sigma\Pi_{sepiolite} = \log((a_{Mg^{2+}} + a_{Ni^{2+}})/(a_{H^+})^2) + (3/2)\cdot\log(a_{SiO_2(aq)}) \quad (4)$$

A given solution characterized by $a_{Mg^{2+}}$, $a_{Ni^{2+}}$, a_{H^+}, and $a_{SiO_2(aq)}$ is represented by a point in the plane of the variables $\log(a_{SiO_2(aq)})$ and $\log((a_{Mg^{2+}} + a_{Ni^{2+}})/(a_{H^+})^2)$. The equilibrium equation for each solid solution is represented in such a diagram by straight lines with equations.

For serpentine-népouite:

$$\log(X_{Mg}\cdot K_1 + (1 - X_{Mg})\cdot K_2) = \log\left(\frac{a_{Mg^{2+}} + a_{Ni^{2+}}}{(a_{H^+})^2}\right) + \frac{2}{3}\cdot\log(a_{SiO_2aq}) \quad (5)$$

For kerolite-pimelite:

$$\log(X_{Mg}\cdot K_3 + (1 - X_{Mg})\cdot K_4) = \log\left(\frac{a_{Mg^{2+}} + a_{Ni^{2+}}}{(a_{H^+})^2}\right) + \frac{4}{3}\cdot\log(a_{SiO_2aq}) \quad (6)$$

For sepiolite-falcondoite:

$$\log(X_{Mg}\cdot K_5 + (1 - X_{Mg})\cdot K_6) = \log\left(\frac{a_{Mg^{2+}} + a_{Ni^{2+}}}{(a_{H^+})^2}\right) + \frac{3}{2}\cdot\log(a_{SiO_2aq}) \quad (7)$$

where X_{Mg} and $(1-X_{Mg})$ are the mole-fractions of Mg and Ni in the solids. Note that K_1, K_2 , ...K_6 represent the equilibrium constants for the reduced formulae of the end-members, as indicated above.

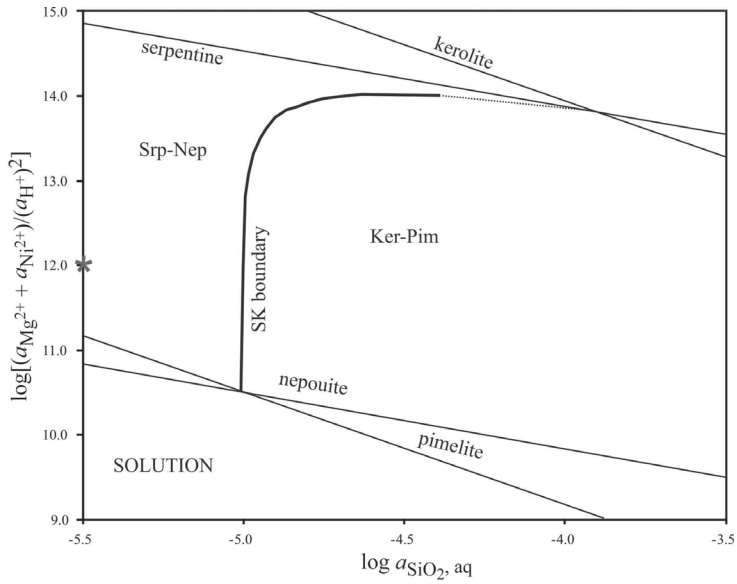

Figure 3. Path followed by the equilibrium between Srp-Nep and Ker-Pim, plotted in the space of log $a_{SiO_2(aq)}$ − log $((a_{Mg^{2+}}+a_{Ni^{2+}})/(a_{H^+})^2)$. A section of the SK curve is metastable (dashed line). The asterisk on coordinates (−5.5, 12) is translated to Lippmann's diagrams in Figure 2a, 2b.

For every point in this diagram, three straight lines cross, corresponding to three possible solid solutions in equilibrium with the solution. However, apart from the boundaries between different phases, only one solid is in equilibrium with the aqueous solution, the other two candidates being undersaturated. Each solid solution (Srp-Nep, Ker-Pim, or Sep-Fal) is defined by a field in the (predominance area) activity diagram [log($a_{SiO_2(aq)}$), log($(a_{Mg^{2+}} + a_{Ni^{2+}})/(a_{H^+})^2$)](see, for instance, Figure 3).

Three-phase equilibria (two solid-solutions and one aqueous solution)

Several authors have described garnierites as an intimate intermixing of two or more Ni-containing phases. The most common association encountered was serpentine-kerolite solid solutions (Vitovskaya *et al.*, 1969; Brindley and Hang, 1973; Wells *et al.*, 2009), but other associations such as chlorite-kerolite, with or without quartz, and a sample composed of sepiolite

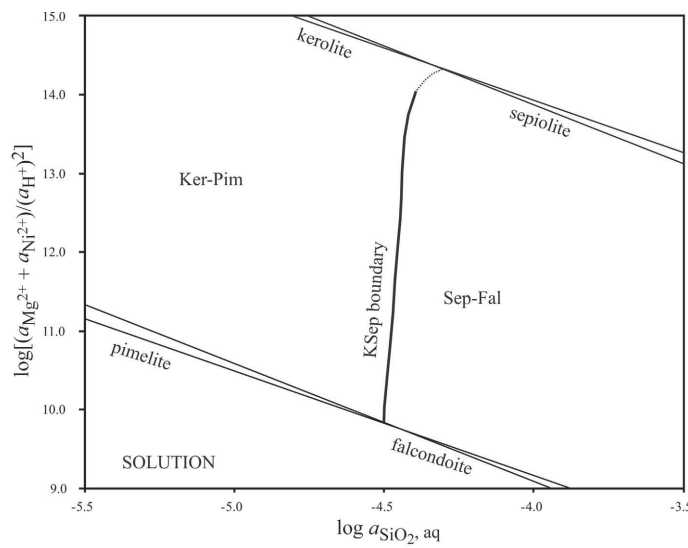

Figure 4. Path followed by the equilibrium between Ker-Pim and Sep-Fal, plotted in the space of log $a_{SiO_2(aq)}$ − log $((a_{Mg^{2+}}+a_{Ni^{2+}})/(a_{H^+})^2)$. A section of the KSep curve is metastable (dashed line).

plus minor serpentine and talc were described by Springer (1974). At a micrometric scale, all these combinations of mineral Ni-bearing phases in Caribbean Ni-laterites have been observed by the present authors. However, not all mixed particulate masses of garnierite are the result of an equilibrium precipitation, so it is important to distinguish the associations that occur as a result of mechanical mixing in breccias or accumulations in fractures, from those that are the result of co-precipitation at near-equilibrium conditions.

Simultaneous precipitation of serpentine-népouite and kerolite-pimelite solid solutions from aqueous solution

When serpentine-népouite and kerolite-pimelite solid solutions precipitate from an aqueous solution in equilibrium, the equilibrium reactions 1, 2, 3, and 4 (Table 2) can be combined to give the equilibrium between the four end-members of both solid solutions. The reaction sought is:

$$MgSi_{2/3}O_{5/3}(OH)_{4/3} + NiSi_{4/3}O_{10/3}(OH)_{2/3} = NiSi_{2/3}O_{5/3}(OH)_{4/3} + MgSi_{4/3}O_{10/3}(OH)_{2/3} \quad (8)$$

and its equilibrium constant is:

$$\log K_{SK} = (1/3)\cdot(\text{Log K1} - \text{Log K2} - \text{Log K3} + \text{Log K4}) = -0.73\pm0.32$$

The path of the solution in equilibrium with the two solid solutions is a curve (SK) that connects the intercept of serpentine-kerolite with that of népouite-pimelite (Figure 3). One section of this curve presents a metastable extension (dashed line, Figure 3). The coordinates of this curve permit the calculation of the total solubility product ($\Sigma\Pi$) of different minerals in the system MgO–NiO–SiO_2–H_2O, and this helps in the characterization of the solutions, in combination with the Lippmann diagrams. For example, the log$\Sigma\Pi$ values corresponding to sepiolite-falcondoite solid solution (equation 4) were plotted on the Lippmann diagram (Figure 2c). All the terms of the Sep-Fal s.s. are undersaturated for all equilibria Srp-Nep+Ker-Pim solid solutions, with the exception of the end near the serpentine-kerolite intercept (Figure 5).

An example of the use of the activity diagram (Figure 3), combined with Lippmann diagrams (Figures 2a and 2b), is as follows. Points falling to the left of the SK curve characterize solutions that will precipitate Srp-Nep s.s. For every point in this field, the log$\Sigma\Pi$ value for Srp-Nep and Ker+Pim can be calculated using equations 2 and 3. For a given value of $\log\Sigma\Pi_{serpentine}$, the corresponding value of $a_{Mg^{2+}}/(a_{Mg^{2+}} + a_{Ni^{2+}})$ is given by the solutus in the corresponding Lippmann diagram. The same activity ratio applied to the Lippmann diagram for kerolite will plot under the solutus, indicating that kerolite s.s. composition is undersaturated. For example, for a point with coordinates (−5.5, 12) (Figure 3), a Srp-Nep crystal is in equilibrium with a solution with an activity ratio $a_{Mg^{2+}}/(a_{Mg^{2+}} + a_{Ni^{2+}})$ of 0.93. The corresponding point in the Lippmann diagram of Ker-Pim s.s. has coordinates (0.93, 4.66), falling under the solutus curve, and then Ker-Pim s.s. would be undersaturated.

Alternatively, the same statement can be inversely formulated: for given values of log$\Sigma\Pi$ and $a_{Mg^{2+}}/(a_{Mg^{2+}} + a_{Ni^{2+}})$, corresponding to an equilibrium Ker-Pim s.s. with solution, a series of (Srp-Nep) s.s. exists and they are supersaturated. This can be demonstrated graphically using the Lippmann diagrams (Figure 2a, 2b).

Similarly, points in the diagram to the right of the SK curve characterize the conditions for equilibrium precipitation of a Ker-Pim s.s.

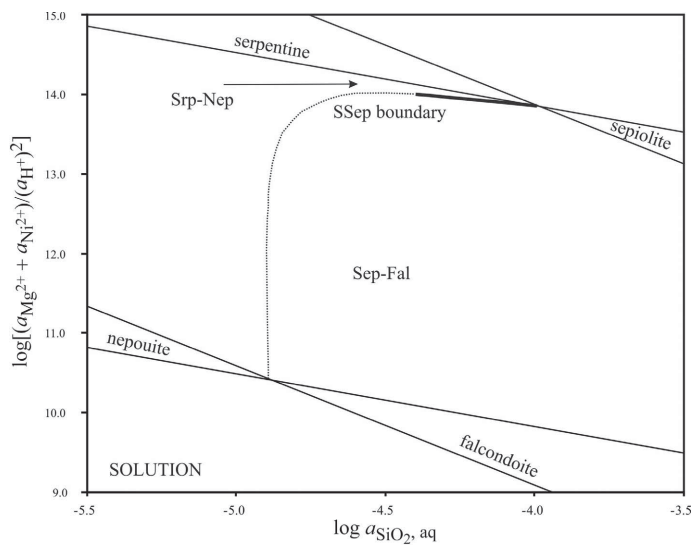

Figure 5. Path followed by the equilibrium between Srp-Nep and Sep-Fal, plotted in the space of log $a_{SiO_2(aq)}$ − log $((a_{Mg^{2+}}+a_{Ni^{2+}})/(a_{H^+})^2)$. A section of the SSep curve is metastable (dashed line).

Simultaneous precipitation of kerolite-pimelite and sepiolite-falcondoite solid solutions from aqueous solution

The equilibrium involved is:

$$MgSi_{4/3}O_{10/3}(OH)_{2/3}\ 1/3H_2O + NiSi_{3/2}O_{15/4}(OH)_{1/2}(H_2O)_{1/2}\cdot H_2O = NiSi_{4/3}O_{10/3}(OH)_{2/3}\ 1/3H_2O + MgSi_{3/2}O_{15/4}(OH)_{1/2}(H_2O)_{1/2}\cdot H_2O\ (\log K_{KSep}) \quad (9)$$

and its equilibrium constant is:

$$\text{Log } K_{KSep} = (1/3)\cdot(\text{Log K3} - \text{Log K4}) + (1/8)\cdot(+\text{Log K6} - \text{Log K5}) = -0.02\pm0.46$$

Using this equilibrium constant for reaction 9, the equilibrium path for these two solid solutions (curve KSep, Figure 4) was constructed on the same basis as curve SK (Figure 3). This curve separates the stability field of Ker-Pim (left) from that of the Sep-Fal.

Along the equilibrium path of Ker-Pim with Sep-Fal, (curve KSep), Srp-Nep s.s. are undersaturated, except for high activity ratios of $X_{Mg^{2+}}$ when they become supersaturated (Figure 5). The corresponding log$\Sigma\Pi$ curve is depicted in Figure 2a.

Simultaneous precipitation of serpentine-népouite and sepiolite-falcondoite solid solutions from aqueous solution

Equilibrium between these solid solutions is given by the reaction:

$$MgSi_{2/3}O_{5/3}(OH)_{4/3} + NiSi_{3/2}O_{15/4}(OH)_{1/2}(H_2O)_{1/2}\cdot H_2O = NiSi_{2/3}O_{5/3}(OH)_{4/3} + MgSi_{3/2}O_{15/4}(OH)_{1/2}(H_2O)_{1/2}\cdot H_2O\ (\log K_{SSep}) \quad (10)$$

The equilibrium constant of this reaction was obtained by proper combinations of the reactions 1 – 2 – 5 + 6 (Table 2), as in the previous examples, yielding log K_{SSep}= −0.76±0.42. The equilibrium path of the equilibrium Srp-Nep+Sep-Fal in the activity diagram is shown in Figure 5. Intimate mixing of these two solid solutions have not been observed. This is consistent with the fact that the curve for Srp-Nep+Sep-Fal equilibrium is metastable, except for the end near the intercept of serpentine-sepiolite (Figure 5). The metastable extension falls in the field of Ker-Pim s.s.: the calculated log$\Sigma\Pi$ for Ker-Pim, translated to the Lippmann diagram lies above the solutus up to an activity ratio $X_{Mg^{2+}}$ near 0.98 (Figure 2b).

Simultaneous precipitation of Ni-bearing sepiolite and quartz

One of the most commonly observed associations in garnierites is the solid solution Sep-Fal with quartz. The equilibrium path in this case is merely the vertical straight line log (a_{SiO_2aq}) = −4.0 corresponding to the solubility of quartz. For greater activities of silica, Sep-Fal s.s. may be associated with amorphous silica.

Whether two solid solutions plus quartz can coexist in equilibrium with an aqueous solution is uncertain. The quartz boundary, represented by a vertical straight line at log(a_{SiO_2}) = −4, intercepts the curve SSep and the metastable extension of KS, in the Mg-rich end of these curves (Figure 6). Two solid solutions plus quartz might precipitate in near-equilibrium conditions. The position of the intersections of pure phase boundaries in the activity diagram and especially their intersections could

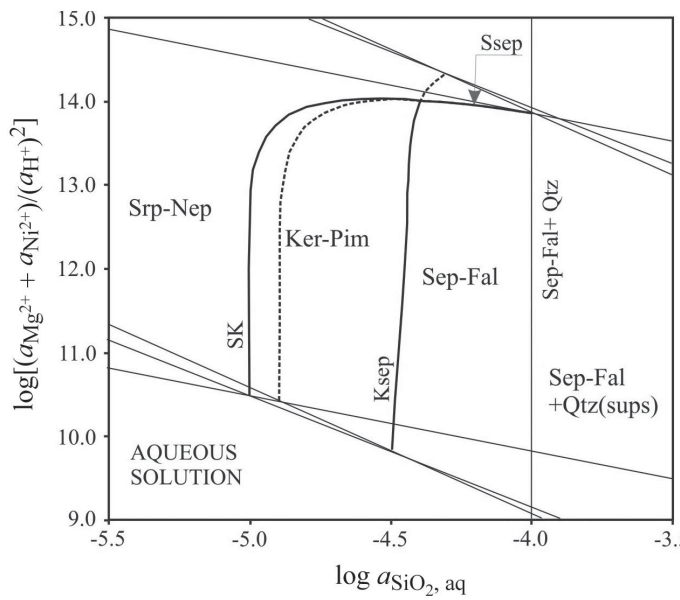

Figure 6. Fields corresponding to the three solid solutions and boundaries: Srp-Nep+Ker-Pim; Ker-Pim+Sep-Fal and Srp-Nep+Sep-Fal. Dashed lines are metastable extensions of these equilibria. Vertical line at log($a_{SiO_2(aq)}$) = −4 gives equilibrium between quartz+Sep-Fal.

change considerably due to uncertainties in the log K values, however.

MATERIALS AND METHODS

For the present study, garnierite samples from the Falcondo (Dominican Republic) and Loma de Níquel (Venezuela) Ni-laterite deposits were selected. The same samples were studied by Proenza *et al.* (2008), Tauler *et al.* (2009), Soler *et al.* (2010), and Villanova-de-Benavent *et al.* (2011a, 2011b). In addition, a list of garnierite minerals from Ni laterites worldwide was compiled in which accurate quantitative electron microprobe data are available (see Figure 1). Garnierites typically precipitate with strong compositional zoning, sometimes with oscillatory content in Ni, and with transitions from one structural type to another (*e.g.* from Ni-serpentine to Ni-kerolite). Thin veinlets of quartz cross the garnierite structures (Tauler *et al.*, 2009; Villanova-de-Benavent *et al.*, 2011b). As both the Lippmann and the activity diagrams were built on the basis of partially theoretically derived equilibrium constants (log K values for Ni end-members), having some experimental control over the reliability of the equilibrium constants used in the graphical representations was considered to be necessary. For this purpose, ~100 polished sections of the material described above were examined to find garnierites consisting of two well characterized phases suitable for detailed chemical analyses, avoiding areas with pronounced zonation and oscillatory composition.

Determination of log K_{SK} from biphasic particulate masses of serpentine-nepouite and kerolite-pimelite solid solutions

A garnierite sample from the Falcondo Mine was a clear example of different generations of co-precipitated Ni-enriched serpentine plus kerolite (Figure 7a). The garnierites consist of homogeneous light green masses cut in places by thin veinlets of quartz (1 mm thick or less) filling fractures or cavities in the saprolite horizon that appeared to have formed under near equilibrium conditions. Under the optical microscope, only quartz veinlets were distinguished from a homogeneous, poorly crystalline yellowish-green mass. Serpentine (mainly lizardite) and talc, in the form of the fine-grained hydrated variety known as kerolite (Brindley *et al.*, 1977), was clearly distinguished by powder X-ray diffraction (XRD). The proportion of phases and the mean size of crystallites were estimated by Rietveld analysis of the XRD profile (Figure 8). Electron microprobe analyses of areas 1–2 μm in size revealed fractions of kerolite together with fractions of serpentine. The TEM studies also showed that the mineral particles were nm-sized (Soler *et al.*, 2008; Villanova-de-Benavent *et al.*, 2011a).

A statistically sufficient number of points analyzed by EMP, in principle, allows the determination as to whether the precipitation of the mixture was produced under equilibrium conditions as well as the composition

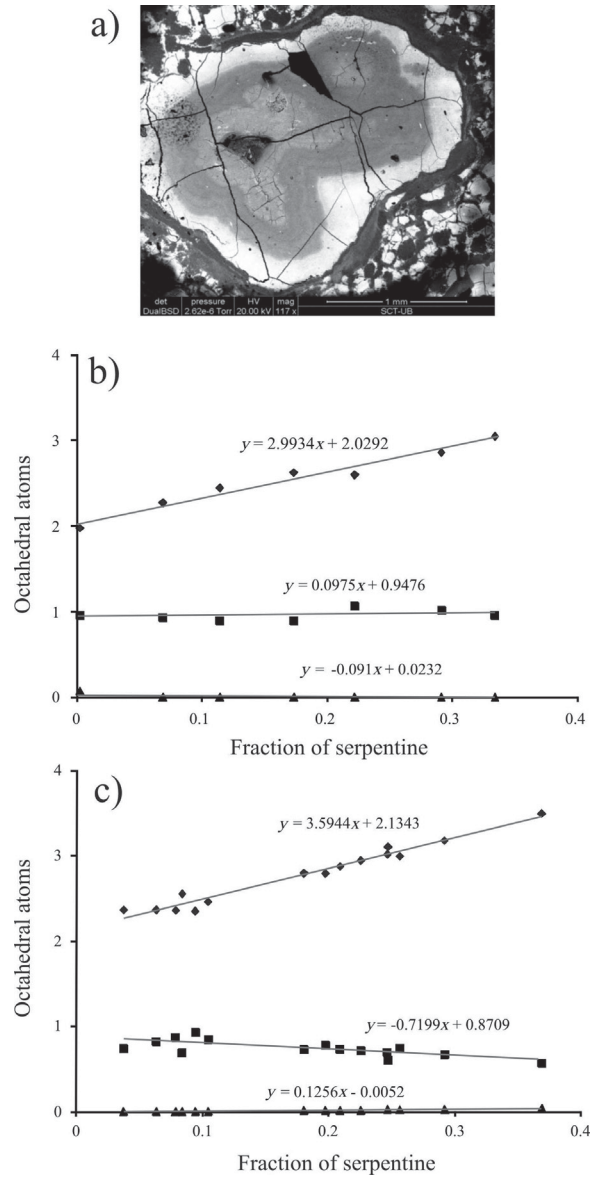

Figure 7. (a) Different generations of kerolite and serpentine with different Ni contents (backscattered electrons). Sample DR1 from Falcondo Mine, Dominican Republic. The analysis given in Table 5 and plotted in Figure 7b corresponds to the inner gray band. (b) Plot of the EMP analyses in the central area of Figure 7a, which consisted of an intermixing of Srp_{84}-Nep_{17} and Ker_{68}-Pim_{32}. Values are octahedral atoms per formula unit (a.p.f.u.) on the basis of four Si. Diamonds: Mg, squares: Ni, triangles: Fe^{2+}. (c) Plot of the EMP analyses of a sample from Loma de Hierro Mine (Venezuela) which consisted of an intermixing of Srp_{95}-Nep_3 and Ker_{71}-Pim_{29}. Values are octahedral a.p.f.u. on the basis of four Si. Diamonds: Mg, squares: Ni, triangles: Fe^{2+}.

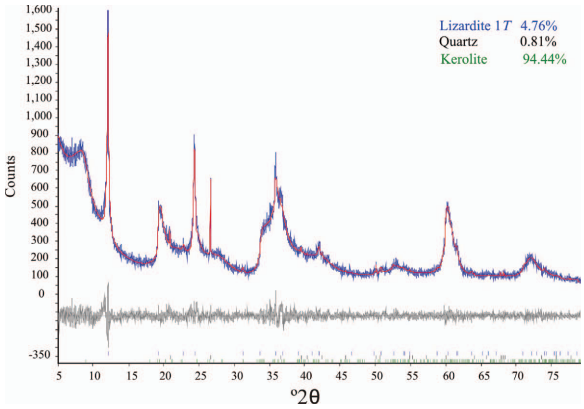

Figure 8. Powder XRD pattern of a garnierite sample DR1 (Falcondo Mine, Dominican Republic), which consisted of co-precipitated serpentine (4.76%), kerolite (94.44%), and 0.81% quartz precipitated in veinlets. The measured profile is represented by the continuous line (Rietveld method); the lower trace represents the difference between measured and calculated profiles; small vertical bars indicate the positions of Bragg reflections.

and the amount of each phase. The composition of each phase gives the distribution of Ni and Mg between them, and the equilibrium constant for the reaction 8. The area illuminated by the electron probe beam includes many particles of both phases in a nm-scale intermixing of serpentine and kerolite s.s. The fraction of each phase can be obtained by adding the atomic coefficient of octahedral atoms, expressing the formula units of both phases on a common number of four Si:

Serpentine s.s.: $(Mg,Ni)_6Si_4O_{10}(OH)_8$
Kerolite s.s.: $(Mg,Ni)_3Si_4O_{10}(OH)_2{\cdot}H_2O$

The fraction of serpentine ($X_{serpentine}$) probed was (Σoctahedral atoms − 3)/3. If simultaneous precipitation of both phases proceeds in equilibrium, all particles of the same phase should have the same composition. For each point analyzed, a given increase in the serpentine fraction represents a constant increase in each octahedral cation (Mg, Ni, Fe^{2+}). Plotting these atomic contents against the serpentine fraction yielded straight lines for Mg, Ni, and Fe^{2+} and the intercepts at $X_{serpentine} = 0$ and $X_{serpentine} = 1$ gave the compositions of (Ker-Pim) s.s. and (Srp-Nep) s.s. in the sample analyzed (Table 5). The reverse was also true: if the atomic contents of substitutable cations failed to lie on straight lines, the probed sample was inhomogeneous and consisted of particles of different compositions.

The log K_{SK} 'analytical' value can be obtained from the composition of the equilibrium phases. For instance, the supposed ideal solid solutions in sample DR1 (Falcondo Mine) (Figure 7b) gave log $K_{SK} = -0.35$, (with $\sigma(\log K_{SK}) = \pm 0.08$) whereas that obtained from the analyses of the sample from Loma de Hierro Mine (Venezuela) (Figure 7c) gave log $K_{SK} = -1.19$ (with $\sigma(\log K_{SK}) = \pm 0.55$). This discrepancy provides a crude approach to the errors involved in the analytical estimation of log K_{SK}. Nevertheless, both 'analytical equilibrium constants' for reaction 8 indicated that Ni atoms are better accommodated in the kerolite structure. These values fall around the value derived theoretically for log K_{SK} (−0.73).

Determination of log K_{KSep} from biphasic particulate masses of kerolite-pimelite and sepiolite-falcondoite solid solutions

The same method was applied to estimate log K_{KSep}. In this case, an homogeneous mass of greenish Ni-bearing minerals from Falcondo Mine were characterized unambiguously as a fine mixture of sepiolite-falcondoite and kerolite-pimelite solid solutions using powder X-ray micro-diffraction on an area of 500 μm (Figure 9) and EMP analyses (Table 6). Diffraction was obtained using a Bruker D8 microdiffraction instrument equipped with a general area detector system (GADDS). As for the Ni-bearing serpentine and kerolite garnierites, the fraction of each phase in each individual analysis (the area illuminated by the electron beam) was obtained readily, expressing the unit formulae on a common basis (the same number of silicon atoms):

Kerolite s.s.: $(Mg,Ni)_9Si_{12}O_{30}(OH)_6{\cdot}3H_2O$
Sepiolite s.s.: $(Mg,Ni)_8Si_{12}O_{30}(OH)_4(H_2O)_4{\cdot}8H_2O$

The fraction of kerolite was then (Σoctahedral cations − 8). The intercepts of the straight lines obtained by plotting Mg, Ni, and Fe^{2+} contents against the fraction of kerolite gave the compositions of both solid solutions. From these, an estimated equilibrium constant for the next reaction (log $K_{KSep} = -0.16$) was obtained. In contrast to the results for the mixtures of serpentine and kerolite, however, the points plotting Mg and Ni against the fraction of kerolite were more dispersed so that the estimation of the equilibrium constant (9) was less reliable. These data show that the sepiolite structure, compared with kerolite, is slightly preferred by Ni.

Analyses of polished sections of garnierites did not reveal biphasic mixtures of serpentine-nepouite and sepiolite-falcondoite solid solutions, so that the equilibrium distribution of Mg and Ni between these phases could not be ascertained analytically. This result is consistent with the narrow calculated stable boundary obtained theoretically for these solid solutions, as discussed below.

RESULTS AND DISCUSSION

By superposing SK, KSep, and SSep boundaries (Figures 3, 4, and 5) a mineral stability diagram for the system MgO–NiO–SiO_2–H_2O was obtained (Figure 6). The six straight lines correspond to the solubilities of the six end-members (Srp, Nep, Ker, Pim, Sep, Fal). Three curves connecting the two intersecting points of pure end-members (curves SK, KSep, and SSep) depict the

Table 5. Analyses of garnierites plotted in Figure 7b, 7c.

	Mg	Al	Si	Ca	Ti	Cr	Mn	Fe	Ni	Mg+Ni+Fe	Serpentine fraction
Falcondo											
DR1_1	1.9739	0.0277	4.0000	0.0097	0.0000	0.0007	0.0000	0.0749	0.9588	3.0076	0.0025
DR1_2	3.1268	0.0229	4.0000	0.0058	0.0008	0.0034	0.0030	0.0407	1.2432	4.4106	0.4702
DR1_3	1.8431	0.0242	4.0000	0.0114	0.0000	0.0019	0.0006	0.0192	1.0512	2.9135	−0.0288
DR1_4	3.0484	0.0194	4.0000	0.0039	0.0000	0.0007	0.0000	0.0000	0.9545	4.0028	0.3343
DR1_5	2.1215	0.0134	4.0000	0.0052	0.0012	0.0006	0.0000	0.0014	0.8765	2.9994	−0.0002
DR1_6	2.8595	0.0149	4.0000	0.0058	0.0000	0.0014	0.0012	0.0000	1.0146	3.8741	0.2914
DR1_7	2.4442	0.0133	4.0000	0.0046	0.0013	0.0014	0.0000	0.0014	0.8973	3.3429	0.1143
DR1_8	2.6257	0.0137	4.0000	0.0044	0.0006	0.0007	0.0000	0.0028	0.8918	3.5202	0.1734
DR1_9	2.2732	0.0126	4.0000	0.0062	0.0012	0.0007	0.0011	0.0014	0.9320	3.2066	0.0689
DR1_10	2.5991	0.0171	4.0000	0.0036	0.0019	0.0027	0.0000	0.0007	1.0662	3.6660	0.2220
Loma de Hierro											
MT_1	2.3602	0.0009	4.0000	0.0000	0.0011	0.0065	0.0000	0.0031	0.8723	3.2357	0.0786
MT_2	2.3669	0.0026	4.0000	0.0000	0.0006	0.0035	0.0000	0.0043	0.8184	3.1896	0.0632
MT_3	2.4614	0.0009	4.0000	0.0000	0.0011	0.0042	0.0010	0.0044	0.8469	3.3128	0.1043
MT_4	2.7949	0.0055	4.0000	0.0000	0.0006	0.0279	0.0022	0.0170	0.7798	3.5917	0.1972
MT_5	2.9445	0.0037	4.0000	0.0000	0.0006	0.0086	0.0022	0.0182	0.7130	3.6758	0.2253
MT_6	2.9932	0.0046	4.0000	0.0000	0.0000	0.0049	0.0016	0.0292	0.7460	3.7685	0.2562
MT_7	3.0171	0.0073	4.0000	0.0000	0.0000	0.0105	0.0000	0.0261	0.6959	3.7390	0.2463
MT_8	2.3492	0.0000	4.0000	0.0000	0.0000	0.0036	0.0000	0.0063	0.9266	3.2822	0.0941
MT_9	2.8752	0.0009	4.0000	0.0000	0.0000	0.0596	0.0000	0.0184	0.7328	3.6264	0.2088
MT_10	2.7970	0.0055	4.0000	0.0000	0.0000	0.0355	0.0000	0.0168	0.7266	3.5404	0.1801
MT_11	3.1769	0.0075	4.0000	0.0000	0.0006	0.0101	0.0006	0.0286	0.6691	3.8746	0.2915
MT_12	3.4957	0.0047	4.0000	0.0000	0.0006	0.0125	0.0027	0.0431	0.5669	4.1057	0.3686
MT_13	3.1042	0.0036	4.0000	0.0000	0.0000	0.0225	0.0000	0.0334	0.6030	3.7406	0.2469
MT_14	2.5535	0.0052	4.0000	0.0000	0.0011	0.0110	0.0020	0.0055	0.6921	3.2511	0.0837
MT_15	2.3647	0.0000	4.0000	0.0000	0.0005	0.0029	0.0010	0.0043	0.7429	3.1118	0.0373

conditions for three phase equilibria (aqueous solution+Srp-Nep+Ker-Pim, *etc.*).

The stability diagram delimits the stability field of each Ni-bearing phyllosilicate and quartz. For each field, only one of these solids is in equilibrium. Along the boundaries delimiting the fields (curves SK, KSep, SSep, and SepQ), two solids are in equilibrium with the solution. Three of these curves intersect at one point (coordinates: −4.3938, 14.0022) which is an invariant point. The solids in equilibrium with the aqueous solution are three solid solutions with calculated compositions: $Srp_{0.747}$-$Nep_{0.253}$, $Ker_{0.353}$-$Pim_{0.647}$, and $Sep_{0.340}$–$Fal_{0.660}$.

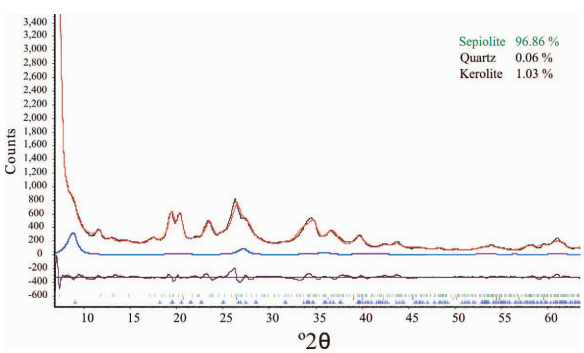

Figure 9. Powder XRD pattern of a mixture of Ker (hydrated talc)-Pim (hydrated willemseite) and Sep-Fal (sample F3 from Falcondo Mine). The measured profile was simulated (continuous line, Rietveld method); the bottom line is the difference between measured and calculated profiles; small vertical bars indicate the positions of Bragg reflections. The detached continuous line is the calculated profile of kerolite.

The proposed activity diagram combined with Lippmann diagrams for each solid solution allows the determination of the main parameters characterizing the solution and the solid in equilibrium, namely, the activity fractions of Mg and Ni in the solids and in the solution, and the silica activity in solution. With a proper speciation model, the amount of Mg, Ni, and Si in solution and the pH can all be obtained.

The exact position of the ends of the boundaries depends on the accuracy of all log K values involved. The equilibrium constants used in this approach have two different origins: experimental for the Mg end-members, and predicted for Ni phases. The differences between experimental values reported by different authors, or values calculated using different models result in a crude estimation of the errors involved. Whenever possible, the analyses of mixtures supposed to

Table 6. Selected analyses of garnierites and mixtures of kerolite-pimelite and sepiolite-falcondoite solid solutions (s.s.).

Label	Na	Mg	Al	Si	K	Ca	Ti	Mn	Fe	Ni	Mg+Fe+Ni	Kerolite fraction
FAL3-1_8	0.0107	2.7178	0.1076	12.0000	0.0106	0.0000	0.0000	0.0000	0.0146	5.3362	8.0685	0.0685
FAL3-1_10	0.0293	3.5487	0.0980	12.0000	0.0193	0.0000	0.0000	0.0128	0.0076	5.4343	8.9907	0.9907
FAL3-1_11	0.0188	3.8942	0.0885	12.0000	0.0309	0.0000	0.0000	0.0041	0.0146	4.5489	8.4577	0.4577
FAL3-1_16	0.0337	1.9725	0.0785	12.0000	0.0369	0.0000	0.0000	0.0000	0.0000	6.4953	8.4678	0.4678
FAL3-1_18	0.0328	2.0216	0.0917	12.0000	0.0086	0.0000	0.0025	0.0029	0.0076	6.0767	8.1059	0.1059
FAL3-1_22	0.0107	2.1790	0.1069	12.0000	0.0175	0.0000	0.0000	0.0000	0.0124	6.0001	8.1914	0.1914
FAL3-1_23	0.0053	2.5447	0.1127	12.0000	0.0105	0.0000	0.0062	0.0093	0.0103	5.5845	8.1395	0.1395
FAL3-1_24	0.0054	2.3785	0.1047	12.0000	0.0071	0.0000	0.0000	0.0000	0.0000	5.7606	8.1392	0.1392
GAR 1-4_10	0.0040	2.8112	0.0000	12.0000	0.0020	0.0109	0.0000	0.0000	0.0000	5.6732	8.4844	0.4844
GAR 1-4_11	0.0040	2.3417	0.0000	12.0000	0.0050	0.0221	0.0060	0.0022	0.0019	6.1426	8.4862	0.4862
GAR 1-5_1	0.0030	3.3612	0.0000	12.0000	0.0000	0.0118	0.0000	0.0023	0.0041	5.0880	8.4533	0.4533
GAR 1-5_1n	0.0030	2.7640	0.0120	12.0000	0.0020	0.0281	0.0020	0.0000	0.0059	5.7792	8.5491	0.5491
GAR 1-5_1q	0.0010	2.6937	0.0000	12.0000	0.0000	0.0027	0.0060	0.0000	0.0075	6.0662	8.7674	0.7674

precipitate in equilibrium were used as a constraint to reduce the choice between different reported or calculated log K values.

The boundary between Srp-Nep and Ker-Pim fields (curve SK) displayed a pronounced change of slope. From the mid point to the Mg end, this boundary was almost parallel to the $\log(a_{SiO_2(aq)})$ axis, so that an increase in the activity of Ni in solution may favor the precipitation of Ker-Pim s.s., because the activity and activity ratio of Ni^{2+} increased downward on the diagram. The mixtures of Srp-Nep+Ker-Pim, fell in a field where the variable $\log((a_{Mg^{2+}} + a_{Ni^{2+}})/(a_{H^+})^2)$ was >13.75, with a Ni/Mg ratio in solution of 10^{-5}–10^{-4} and calculated pH of ~9.2. The section of the SK boundary between the invariant point and the serpentine-kerolite intercept was metastable, running almost coincidental with, but below, the stable SSep boundary. For $\log((a_{Mg^{2+}} + a_{Ni^{2+}})/(a_{H^+})^2)$ values of <13, in the Ni-rich portion, the boundary SK was parallel to the vertical axis, and only the activity of silica determined the type of solid solution that precipitates. This was also the case for the next boundary between Ker-Pim and Sep-Fal (curve KSep) which drew an almost straight vertical line at $\log(a_{SiO_2(aq)}) = -4.5$. The portion of the Srp-Nep field limiting with the Sep-Fal field was very narrow (boundary curve SSep), making the co-precipitation of these minerals less probable. In fact, coexistence of these two solid solutions was not observed in any of the samples.

Many processes leading to the formation of garnierites depend on factors not treated in this work (kinetic, climatic, hydrologic, tectonic, *etc.*). The stability diagram constructed (Figure 6) suggested, however, that two main temporal and spatial trends were related to the formation of Ni-enriched supergene phases. An increase in Ni^{2+} in the solutions percolating through or contained within the altered parent rock may be explained by one or the other of these two mechanisms, *e.g.* the leaching of Ni from goethite in the limonitic horizon by meteoric waters, and the repeated cycle of congruent dissolution of Ni-poor phyllosilicates followed by equilibrium precipitation of a phyllosilicate, slightly richer in Ni. On the other hand, an increase in the silica activity may have occurred with the formation of a great variety of different forms of silicification (Golightly, 1981; Freyssinet *et al.*, 2005; Trescases, 1975). Soler *et al.* (2008) observed in flow-through dissolution experiments of garnierites at low pH that the initial aqueous ratios of Mg/Si and (Mg+Ni)/Si were three times greater than in the solid. After 900 h, these ratios decreased to values only slightly above those of the dissolving garnierite. For higher pH values, the ratios in solution were always a little higher than in the dissolving phase. Preferential release of Mg over Si has been observed in Mg-phyllosilicates previously (see Soler *et al.*, 2008). Jurinski and Rimstidt (2001) observed the formation of a silica-rich surface on dissolving mineral grains. These experiments highlighted the fact that, for short dissolving events (*i.e.* a short period of rain), the dissolution of Ni-bearing phyllosilicates would not be stoichiometric with respect to the (Mg+Ni)/Si ratios but would be stoichiometric with respect to the Mg/Ni ratio. As a result, significant amounts of silica might accumulate and remain available until changes in pH allow its mobilization. In turn, the supply of silica to aqueous solutions explains the increase in the silica activity and the evolution of garnierites from Ni-serpentines to Ni-sepiolites. In summary, the evolution of garnierites, as shown in the stability diagram (Figure 6), may be depicted as a trend pointing downward (Ni enrichment) and to the right (increase in silica activity).

CONCLUSIONS

Garnierites are very often composed of an intimate mixture of Ni-enriched phyllosilicates which include serpentine-népouite, kerolite-pimelite, and sepiolite-falcondoite solid solutions. The variable and intricate

textures on a scale of only tens of microns (massive, accordion-like, layered, brecciated, *etc.*) represent an additional barrier to understanding the formation and evolution of these ore minerals. New insights were gained on the basis of the equilibrium thermodynamics approach presented above.

The dissolution equilibrium constants for pure Ni end-members népouite, pimelite, and falcondoite were derived following the method proposed by Nriagu (1975). These log K values, together with selected experimental dissolution constants for pure Mg end-members (serpentine, kerolite, and sepiolite) drawn from the literature, constitute a useful array of thermodynamic data.

The log K values for the six Mg-Ni end-members allows the calculation of the solidus and solutus curves of the Lippmann diagrams for the solid solutions serpentine-népouite, kerolite-pimelite, and sepiolite-falcondoite, assuming ideal solid solutions.

In Ni laterite soils, the mechanism of supergene enrichment consists of congruent dissolution of Ni-poor primary minerals followed by near-equilibrium precipitation of secondary Ni-enriched hydrated phyllosilicates. This was illustrated readily using Lippmann diagrams. This mechanism can operate through several cycles of congruent dissolution-equilibrium precipitation. The percolating aqueous solutions can also be enriched in Ni by the leaching of goethite.

The stability fields of each solid solution and the boundaries between them can be represented in [log $a_{SiO_2(aq)}$, log $((a_{Mg^{2+}} + a_{Ni^{2+}})/(a_{H^+})^2)$] diagrams. These activity diagrams, combined with Lippmann diagrams provide an almost complete characterization of the aqueous and solid(s) solution(s) in equilibrium.

After congruent dissolution of primary Ni-bearing minerals, the poor mobility of silica leads to progressive silicification within the laterite profile. The silica activity increases with time and through the profile, reaching saturation or supersaturation levels. The precipitation of Ni ore is then characterized by a succession of mineral phases progressively enriched in Ni and with more Si. Secondary Ni serpentines are the first phases to precipitate, followed by Ni-kerolite and Ni-sepiolite-like minerals.

ACKNOWLEDGMENTS

This research was supported financially by the Spanish projects CGL2006-07384 and CGL2009-10924 and grant 2009-SGR444 of the Catalonian Government. Paul Golightly and an anonymous reviewer are acknowledged for their constructive criticism which improved the manuscript. JAP and JFL gratefully acknowledge the help and hospitality extended by the staff at FalcondoXSTRATA mine. In particular they thank Francisco Longo for his help in collecting the garnierites at Falcondo Mine. The authors also acknowledge the assistance of X. Llovet (Centres Científics i Tecnolgics of the Universitat de Barcelona) for his assistance with the electron micoprobe analyses.

REFERENCES

Brand, N.W., Butt, C.R.M., and Elias, M. (1998) Nickel laterites: classification and features. *AGSO Journal of Australian Geology and Geophysics*, **17**, 81–88.

Bricker, O.P., Nesbitt, H.W., and Gunter, W.D. (1973) The stability of talc. *American Mineralogist*, **58**, 64–72.

Brindley, G.W. and Hang, P.T. (1973) The nature of garnierites – I. Structures, chemical composition and color characteristics. *Clay and Clay Minerals*, **21**, 27–40.

Brindley, G.W. and Maksimovic, Z. (1974) The nature and nomenclature of hydrous nickel-containing silicates. *Clay Minerals*, **10**, 271–277.

Brindley, G.W. and Wan, H.M. (1975) Composition structures and thermal behavior of nickel containing minerals in the lizardite-népouite series. *American Mineralogist*, **60**, 863–871.

Brindley, G.W., Bish, D.L., and Wan, H.M. (1977) The nature of kerolite, its relation to talc and stevensite. *Mineralogical Magazine*, **41**, 443–452.

Brindley, G.W., Bish, D.L., and Wan, H.M. (1979) Compositions, structures and properties of nickel containing minerals in the kerolite-pimelite series. *American Mineralogist*, **64**, 615–625.

Christ, C.L., Hostetler, P.B., and Siebert, R.M. (1973) Studies in the system $MgO\text{-}SiO_2\text{-}CO_2\text{-}H_2O$ (III): The activity-product constant of sepiolite. *American Journal of Science*, **273**, 65–83.

Cluzel, D. and Vigier, B. (2008) Syntectonic mobility of supergene nickel ores from New Caledonia (Southwest Pacific). Evidence from faulted regolith and garnierite veins. *Resource Geology*, **58**, 161–170.

Evans, B.W. (2004) The serpentinite multisystem revisited: chrysotile is metastable. *International Geology Review*, **46**, 479–506.

Freyssinet, Ph., Butt, C.R.M., and Morris, R.C. (2005) Ore-forming processes related to lateritic weathering. *Economic Geology 100th Anniversary Volume*, 681–722.

Gleeson, S.A., Butt, C.R., and Elias, M. (2003) Nickel laterites: A review. *SEG Newsletter*, **54**, 11–18.

Glynn, P.D. and Reardon, E.J. (1990) Solid-solution aqueous-solution equilibria: thermodynamic theory and representation. *American Journal of Science*, **290**, 164–201.

Golightly, J.P. (1981) Nickeliferous Laterite Deposits. *Economic Geology, 75th Anniversary Volume*, 710–735.

Golightly, J.P. (2010) Progress in understanding the evolution of nickel laterite. *2010 Society of Economic Geology, Inc. Special Publication*, **15**, 451–485.

Helgeson, H.C. (1969) Thermodynamics of hydrothermal systems at elevated temperatures and pressures. *American Journal of Science*, **169**, 729–804.

Helgeson, H.C., Delany, J.M., Nesbitt, H.W., and Bird, D.K. (1978) Summary and critique of the thermodynamic properties of rock-forming minerals. *American Journal of Science*, **278-A**, 227 pp.

Hostetler, P.B. and Christ, C.L. (1968) Studies in the system $Mg\text{-}SiO_2\text{-}CO_2\text{-}H_2O$ I: the activity product constant of chrysotile. *Geochimica et Cosmochimica Acta*, **32**, 482–497.

Jurinski, J.B. and Rimstidt, J.D. (2001) Biodurability of talc. *American Mineralogist*, **86**, 392–399.

Lewis J.F., Draper, G., Proenza, J.A., Espaillat, J., and Jimenez, J. (2006) Ophiolite related ultramafic rocks (serpentinites) in the Caribbean region: a review of their occurrence, composition, origin, emplacement and Ni-laterite soils formation. *Geologica Acta*, **4**, 237–263

Lippman, F. (1980) Phase diagrams depicting the aqueous solubility of binary mineral systems. *Neues Jahrbuch für Mineralogie Abhandlung*, **139**, 1–25.

Manceau, A. and Calas, G. (1985) Heterogeneous distribution of nickel in hydrous silicates from New Caledonia ore deposits. *American Mineralogist*, **70**, 549–558.

Manceau, A., Calas, G., and Decarreau, A. (1985) Nickel-bearing clay minerals: I. Optical spectroscopic study of nickel crystal chemistry. *Clay Minerals*, **20**, 367–387.

Manceau, A., Tamura, N., Celestre, R.S., MacDowell, A.A., Geoffroy, N., Sposito, G., and Padmore, H.A. (2003) Molecular-scale speciation of Zn and Ni in soil ferromanganese nodules from loess soils of the Mississippi Basin. *Environmental Science & Technology*, **37**, 75–80.

Mel'nik, Y.P. (1972) *Thermodynamic Constants for the Analysis of Conditions of Formation of Iron Ores (in Russian)*. Institute of the Geochemistry and Physiscs of Minerals, Academy of Sciences, Ukranian S.S.R. Kiev, 193 pp.

Nriagu, J.O. (1975) Thermochemical approximation for clay minerals. *American Mineralogist*, **60**, 834–839.

Pelletier, B. (1983) Localisation du nickel dans les minerais ''garnieritiques'' de Nouvelle-Caledonie. *Sciences Géologique: Mémoires*, **73**, 173–183.

Phillips, S.L., Hale, F.V., Silvester, L.F., and Siegel, M.D. (1988) *Thermodynamic Tables for Nuclear Waste Isolation. Aqueous Solution Database, Vol. 1*. Lawrence Berkeley Laboratory, Berkeley, California and Sandia National Laboratories, Albuquerque, New Mexico, USA.

Prieto, M. (2009) Thermodynamics of solid solution-aqueous solution systems. Pp. 47–85 in: *Thermodynamics and Kinetics of Water-Rock Interaction*. Reviews in Mineralogy & Geochemistry, **70**, Mineralogical Society of America, Washington, D.C.

Proenza, J.A., Lewis, J.F., Galí, S., Tauler, E., Labrador, M., Melgarejo, J.C., Longo, F., and Bloise, G. (2008) Garnierite mineralization from Falcondo Ni-laterite deposit (Dominican Republic). *Macla*, **9**, 197–198.

Reddy, B.J., Frost, R.L., and Dickfos, M.J. (2009) Characterisation of Ni silicate-bearing minerals by UV-vis-NIR spectroscopy. Effect of Ni substitution in hydrous Ni-Mg silicates. *Spectrochimica Acta*, **A71**, 1762–1768.

Soler, J.M., Cama, J., Galí, S., Meléndez, W., Ramírez, A., and Estanga, J. (2008) Composition and dissolution kinetics of garnierite from the Loma de Hierro Ni-laterite deposit, Venezuela. *Chemical Geology*, **249**, 191–202.

Springer, G. (1974) Compositional and structural variations in garnierites. *The Canadian Mineralogist*, **12**, 381–388.

Springer, G. (1976) Falcondoite, nickel analogue of sepiolite. *The Canadian Mineralogist*, **14**, 407–409.

Stoesell, R.K. (1988) 25ºC and 1 atm dissolution experiments of sepiolite and kerolite. *Geochimica et Cosmochimica Acta*, **52**, 365–374.

Tauler, E., Proenza, J.A., Galí, S., Lewis, J.F., Labrador, M., García-Romero, E., Suarez, M., Longo, F., and Bloise, G. (2009) Ni-sepiolite-falcondoite in garnierite mineralization from the Falcondo Ni-laterite deposit, Dominican Republic. *Clay Minerals*, **44**, 435–454.

Tardy, Y. and Duplay, J. (1992) A method of estimating the Gibbs energies of formation of hydrated and dehydrated clay minerals. *Geochimica et Cosmochimica Acta*, **56**, 3007–3029.

Tardy, Y. and Garrels, R.M. (1974) A method of estimating the Gibbs energies of formation of layer silicates. *Geochimica et Cosmochimica Acta*, **38**, 1101–1116.

Trescases, J.J. (1975) *L'évolution géochimique supergène des roches ultrabasiques en zone tropicale: Formations des gisements nickeliferes de Nouvelle Calédonie*. Editions ORSTOM, Paris, 259 pp.

Villanova-de-Benavent, C., Nieto, F., Proenza, J.A., and Galí, S. (2011a) Talc- and serpentine-like "garnierites" from Falcondo Ni-laterite deposit (Dominican Republic): a HRTEM approach. *Macla*, **15**, 197–198.

Villanova-de-Benavent, C., Proenza, J.A., Galí, S., Tauler, E., Lewis, J.F., and Longo, F. (2011b) Talc- and serpentine-like "garnierites" in the Falcondo Ni-laterite deposit, Dominican Republic. 'Let's talk ore deposits', 11th Biennial Meeting SGA 2011, Antofagasta, Chile, 3 pp.

Vitovskaya, I.V., Berkhin, S.I., and Yashina, R.S. (1969) The serpentine component of nickel silicates. *Doklady Akademie Nauk SSSR*, **189**, 160–162.

Wagman, D.D., Evans, W.H., Parker, U.B., Halow, I., Bailey S.M., and Schumm, R.H. (1968) Selected values of chemical thermodynamic properties. *National Bureau of Standards Technical Note*, 270–3 (1968), 270–4 (1969).

Wells, M.A., Ramanaidou, E.R., Verrall, M., and Tessarolo, C. (2009) Mineralogy and crystal chemistry of "garnierites" in the Goro lateritic nickel deposit, New Caledonia. *European Journal of Mineralogy*, **21**, 467–483.

(*Received 27 October 2011; revised 21 March 2012; Ms. 626; A.E. W.D. Huff*)